PUBLICATIONS OF THE ASTRONOMICAL SOCIETY OF THE PACIFIC, **122**:451–469, 2010 April


# Design Overview and Performance of the WIYN[1] High Resolution Infrared Camera (WHIRC)

MARGARET MEIXNER,[2,3] STEPHEN SMEE,[4] RYAN L. DOERING,[2,3,5,6] ROBERT H. BARKHOUSER,[4]
TODD MILLER,[2] JOSEPH ORNDORFF,[4] PATRICIA KNEZEK,[7,8] ED CHURCHWELL,[5]
GREGG SCHARFSTEIN,[4] JEFFREY W. PERCIVAL,[5] DAVID MILLS,[8]
CHARLES CORSON,[8] AND RICHARD R. JOYCE[8]

*Received 2009 December 4; accepted 2010 February 8; published 2010 March 19*

**ABSTRACT.** We present the design overview and on-telescope performance of the WIYN High Resolution Infrared Camera (WHIRC). As a dedicated near-infrared (0.8–2.5 $\mu$m) camera on the WIYN Tip-Tilt Module (WTTM) port, WHIRC can provide near-diffraction-limited imaging with an FWHM of $\sim 0.25''$ at $K_s$ with active WTTM correction and does deliver typical imaging with an FWHM of $\sim 0.6''$ without WTTM. WHIRC uses a $2048 \times 2048$ HgCdTe array from Raytheon's VIRGO line, which has been developed for the VISTA project. The WHIRC filter complement includes *J*, *H*, $K_s$, and 10 narrowband filters. WHIRC's compact design makes it the smallest near-infrared camera with this capability. We determine a gain of $3.3 \pm 0.2$ e$^-$ ADU$^{-1}$ via a photon transfer analysis and a readout noise of $\sim 19$ e$^-$. A measured dark current of $0.13$ e$^-$ s$^{-1}$ indicates that the cryostat is extremely light tight. A plate scale of $0.099'' \times 0.10''$ pixel$^{-1}$ results in a field of view (FOV) of $3.3' \times 3.4'$, which is a compromise between the highest angular resolution achievable and the largest FOV correctable by WTTM. Measured throughput values ($\sim 0.27 \pm 0.02$ in $H$ band) are consistent with those predicted for WHIRC based on an analysis of individual optical elements and detector quantum efficiency (QE). WHIRC's photometric quality is better than $\sim 0.02$ magnitudes in all bands. WHIRC is a general use instrument at the WIYN telescope enabling high-definition near-infrared imaging studies of a wide range of astronomical phenomena including star formation regions, stellar populations, and interstellar medium in nearby galaxies, high-$z$ galaxies, and transient phenomena.

*Online material:* color figures

## 1. INTRODUCTION

The 8–10 m class telescopes (e.g., Gemini, Keck, VLT, Subaru) are well equipped with near-infrared (NIR) instruments but access to these telescopes is very limited. Many projects may be more appropriately carried out with 4 m class telescopes equipped with NIR instruments that have a unique filter selection and moderately wide fields than with deeper, narrow fields on 8–10 m telescopes. Indeed, large-scale survey imaging projects performed with NIR cameras on 4 m telescopes will provide an excellent basis for spectroscopic projects on 8–10 m telescopes. Moreover, *Spitzer*, SOFIA, Herschel, and *James Webb Space Telescope* (*JWST*) provide great pressure on ground-based telescopes for follow-up complementary observations.

The WIYN telescope is an active 3.5 m telescope (e.g., Johns & Blanco 1994; Roddier et al. 1995; Anderson et al. 1994) located at an excellent seeing site on Kitt Peak, operated by the University of Wisconsin, Indiana University, Yale University, and the National Optical Astronomical Observatory (NOAO).[9] The WIYN Tip-Tilt Module (WTTM) provides near-diffraction-limited imagery from 0.4 to 2.5 $\mu$m on WIYN (Claver et al. 2003). WTTM has demonstrated its ability

[1] The WIYN Observatory is a joint facility of the University of Wisconsin-Madison, Indiana University, Yale University, and the National Optical Astronomy Observatories.

[2] Space Telescope Science Institute, 3700 San Martin Drive, Baltimore, MD; meixner@stsci.edu, jmiller@stsci.edu.

[3] Visiting Astronomer, Kitt Peak National Observatory, National Optical Astronomy Observatories, which is operated by the Association of Universities for Research in Astronomy, Inc. (AURA) under cooperative agreement with the National Science Foundation.

[4] Instrument Development Group, Johns Hopkins University, Homewood Campus, Baltimore, MD; smee@pha.jhu.edu, barkhouser@pha.jhu.edu, orndorff@pha.jhu.edu, gregory@flexurellc.com.

[5] Department of Astronomy, University of Wisconsin-Madison, 475 North Charter Street, Madison, WI; doering@astro.wisc.edu, ebc@astro.wisc.edu, jwp@sal.wisc.edu.

[6] Department of Physics, University of Illinois, Urbana, IL.

[7] WIYN Observatory, Tucson, AZ.

[8] National Optical Astronomical Observatory (NOAO), Tucson, AZ; pknezek@noao.edu, corson@noao.edu, dmills@noao.edu, joyce@noao.edu.

[9] At http://www.wiyn.org/.

to improve the image quality of the WIYN telescope at $R$ band by decreasing the FWHM from 0.71″ to 0.53″. Tip-tilt correction is expected to have its maximum benefits in the NIR for a 3.5 m class telescope (Roddier et al. 1991). The excellent intrinsic image quality provided by the WIYN 3.5 m telescope, coupled with the WTTM, provided an exceptional opportunity for WIYN to expand its capabilities into the NIR with near-diffraction-limited imaging over a 3′ FOV. Indeed, it was always recognized that a logical upgrade path leading to maximized scientific payback was to provide a state-of-the-art NIR camera.

Pilot studies of WIYN's NIR imaging capability were performed with NIRIM (Meixner et al. 1999), which was on temporary loan to WIYN, and demonstrated that an image quality of ∼0.5″ was typical and that ∼0.3″ was achievable without active correction (Meixner et al. 2004). The excellent image quality of NIRIM on WIYN enabled an unconfused detection of the massive protostar in G192.2 (Indebetouw et al. 2003) and permitted a detailed study of photodissociation regions in the planetary nebula NGC 6720 (Speck et al. 2003) and an NIR photometry and imaging study of 35 Herbig Ae/Be candidate stars (Doering and Meixner 2009). The NIRIM pilot studies and the WTTM performance motivated the creation of the WIYN High Resolution Infrared Camera (WHIRC): a dedicated NIR (0.8–2.5 $\mu$m) camera on the WTTM port in order to provide near-diffraction-limited imaging with an FWHM of ∼0.25″ in $K_s$ with active WTTM correction.

WHIRC was delivered to WIYN in 2007 July for integration and testing with WIYN, opened for shared risk use in spring 2008, and accepted as a general use instrument by the WIYN board in 2008 October. WHIRC is permanently mounted on the WTTM port of WIYN. Observers have the option of doing direct imaging or tip-tilt corrected imaging with WTTM+ WIYN. This article describes the design overview of WHIRC and its performance on the WIYN telescope. The detailed optical and mechanical design is described by S. A. Smee, R. H. Barkhouser, G. A. Scharfstein, M. Meixner, J. D. Orndoff, T. Miller (2010, in preparation). Initial descriptions of the design and its considerations were presented previously at SPIE meetings by Meixner et al. (2004) and Barkhouser et al. (2004), and preliminary performance characteristics were presented by Meixner et al. (2008). This article is outlined as follows: § 2 reviews the science drivers for the project; § 3 provides a system level view of WHIRC's design and major subsystems; § 4 covers WHIRC's detector performance and resulting instrument sensitivity on WIYN; and § 5 reports on WHIRC's imaging and photometric qualities. In § 6, we summarize with a discussion of WHIRC's capabilities in comparison to other comparable instruments.

TABLE 1
WHIRC Imaging Features

| Instrument Parameter | Value | |
|---|---|---|
| Detector type | Raytheon/VIRGO HgCdTe array | |
| Size (pixels) | 2048 × 2048 | |
| Pixel pitch ($\mu$m) | 20 | |
| Wavelengths ($\mu$m) | 0.8–2.5 | |
| Image scale (arcseconds pixel$^{-1}$) | 0.099 × 0.10 | |
| Field of view (′) | 3.3 × 3.4 | |
| Best measured PSF FWHM (″) | 0.28 | |
| Typical measured PSF FWHM (″) | 0.6 | |
| Filters: | $\lambda_0$ ($\mu$m) | $\Delta\lambda/\lambda$ |
| MKO[a] $J$ | 1.25 | 0.162 |
| MKO[a] $H$ | 1.644 | 0.300 |
| MKO[a] $K_s$ | 2.15 | 0.343 |
| Low airglow | 1.061 | 0.0132 |
| He I | 1.083 | 0.0094 |
| Pa $\beta$ | 1.284 | 0.0158 |
| Pa $\beta$ (∼4500 km s$^{-1}$)[b] | 1.30 | 0.0133 |
| [Fe II] | 1.646 | 0.0164 |
| [FeII](∼4500 km s$^{-1}$)[b] | 1.671 | 0.0162 |
| $H_2$ | 2.12 | 0.0216 |
| Br $\gamma$ | 2.16 | 0.0215 |
| Br $\gamma$ (∼4500 km s$^{-1}$)[b] | 2.19 | 0.0237 |
| CO | 2.295 | 0.0228 |

[a] MKO stands for Mauna Kea Observatories NIR filter set as defined by Tokunaga et al. 2002.

[b] The (∼4500 km s$^{-1}$) means redshifted to an equivalent recessional velocity of ∼4500 km s$^{-1}$.

## 2. SCIENCE DRIVERS

WHIRC was designed to support the full range of scientific interests in high-definition NIR imaging that may be proposed by the WIYN community, including the general astronomical community through NOAO. The WHIRC science team identified four science interests that defined the instrument capabilities and filter complement: follow-up to the *Spitzer* surveys of the Milky Way's Galactic star formation and evolved stars, studies of nearby galaxies, and identification of high-$z$ galaxies and transient phenomena.

### 2.1. Milky Way Star Formation and Stellar Feedback

The *Spitzer* Legacy programs that concentrated on imaging the Milky Way, e.g., Galactic Legacy Infrared Mid-Plane Survey Extraordinaire (GLIMPSE; Churchwell et al. 2009; Benjamin et al. 2003), have studied the stellar populations of the Milky Way with a scientific emphasis on star formation. GLIMPSE detected thousands of infrared dark clouds (IRDCs), the primary stellar nurseries of massive stars in the Galaxy. WHIRC provides an angular resolution of ∼0.25″ or ∼4 AU at 1 kpc permitting better photometry measurements of these confusion and background limited regions. With WHIRC, it will be possible to obtain accurate photometry at $J$, $H$, and $K_s$ down to spectral types ∼K0V, K0V–K5V, and late GV stars, respectively, at the center of dense clusters like Westerlund 2, which illuminates RCW49, at distances of 4–5 kpc and $A_V = 5$ mag. High spatial resolution images over large fields of view with narrowband filters are key to understanding the

interactions of massive star feedback to the surrounding interstellar medium. GLIMPSE has identified candidate jets, and bowshocks, and bubbles associated with star formation regions that can be studied by WHIRC in the Pa$\beta$, Br$\gamma$, $H_2$, and [Fe II] filters, with associated narrowband continuum filters. GLIMPSE has also imaged candidate planetary nebulae, which could be differentiated from H II regions using the He I filter. The interaction of supernovae remnants, imaged by GLIMPSE, with the ambient interstellar matter (ISM) could be far better defined and studied with high-resolution WHIRC NIR images in shock tracers such as [Fe II] and $H_2$. Coverage of the GLIMPSE regions requires operational procedures for dithering, to mitigate detector artifacts, and mosaicking in order to create the necessary large FOVs.

### 2.2. Nearby Galaxies

WHIRC offers the angular resolution ($0.25'' = 20$ pc at $D = 10$ Mpc) and sensitivity to open a new window on the systematic analysis of evolved stellar populations in the nearby universe. With a limiting magnitude of $H = 22.5$ in ~45 minutes of onsource integration, WHIRC can reach to below the red giant branch (RGB) tip with $M_H = -6$ for $D < 4$ Mpc and red supergiants (RSGs) with $M_H = -9$ to at least 10 Mpc (limited by resolution). It will be a powerful stellar populations machine that can be applied to RGB and asymptotic giant branch (AGB) studies (distances, metallicities, star formation histories; e.g., Harbeck et al. 2004) in nearby galaxy groups. The RSGs will allow star-forming patterns to be traced and the evolution of massive stellar populations explored in more than 100 galaxies. Super star clusters (SSCs) of $10^5 M_\odot$ and 10 Myr will have $M_H \sim -15$ and can be observed to $D \sim 50$ Mpc, with the distance limit set by crowding. WHIRC images with the CO and $K_s$ filters can identify the number of RSGs and thus help assess the ages of such compact clusters.

With WHIRC, regions of intense star formation in environments from galactic centers to major starbursts will be subject to routine scrutiny. Analysis of the WHIRC images will reveal distributions, intensities, and extinction of major star-forming sites and provide targets for spectrophotometric and multiwavelength follow-up. Scientific objectives of this work are to demonstrate that starbursts are not just scaled-up versions of spiral disks, e.g., due to the presence of associations of SSCs that make starburst clumps. The next steps, where WHIRC is critical, is to determine the astrophysical implications of this kind of star

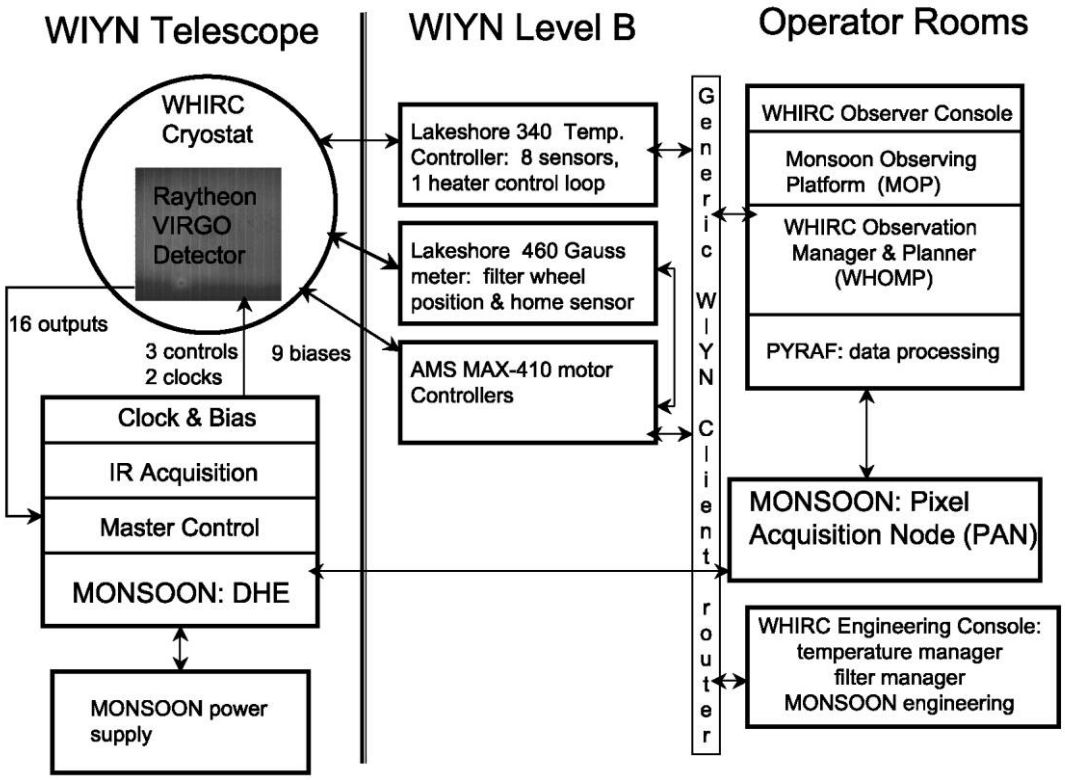


FIG. 1.—WHIRC system block diagram showing the major subsystem components, where they are distributed, and the communication paths in the system. See the electronic edition of the PASP for a color version of this figure.

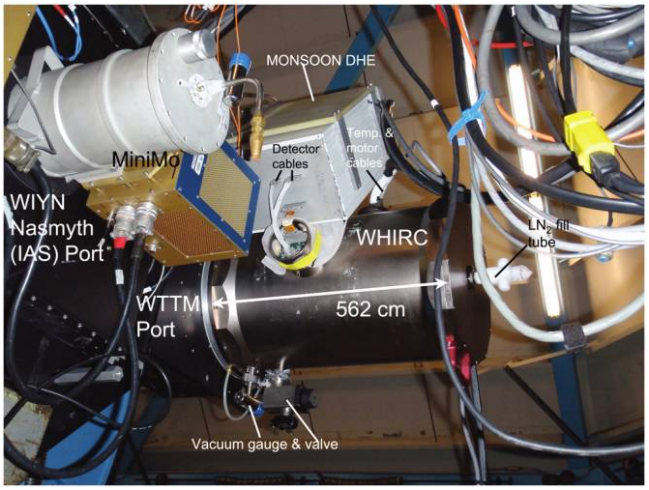


FIG. 2.—WHIRC cryostat mounted on the WTTM port at WIYN. Labels identify the detailed features of WHIRC, as well as its size. WHIRC's associated MONSOON DHE are mounted on a bracket attached to the instrument adapter system (IAS) to alleviate the moment arm loading on WTTM. The neighboring instrument, MiniMo, is located on the WIYN Nasmyth port, also known as the IAS port at WIYN. A mirror slide picks off the light from the IAS port and redirects it to the WTTM port. This ability allows sequential, but not simultaneous, observations with both instruments during a night.

formation for the evolution of the host galaxy and injection of gas from the starburst into its surroundings. WHIRC images of the gas environments of these starbursts in the $4500\ \mathrm{km\,s^{-1}}$ redshifted filters of Pa$\beta$, [Fe II], and Br$\gamma$ will reveal the energetics and physical properties of these dust enshrouded starburst regions.

### 2.3. High-$z$ Galaxies

Wide and deep field surveys for high-$z$ galaxies in blank sky regions have been performed with the NASA great observatories, *Hubble Space Telescope* (*HST*), *Chandra*, and *Spitzer*. The availability of NIR data is essential for galaxy studies in order to constrain the spectral energy distribution, improve photometric redshifts, and identify extremely red objects and possibly very high-$z$ galaxy candidates. WHIRC will allow us to obtain high-resolution NIR images over large fields. By resolving galaxies at low-to-intermediate redshift ($z = 0.7$–$2.0$) one would be able to carry out SED-based population synthesis within a galaxy and begin to test the assembly history of galaxies. Images of these same galaxies in the low airglow filter at 1.06 $\mu$m will permit studies of star formation activity in discrete redshift windows corresponding to H$\alpha$, [O III], and [O II].

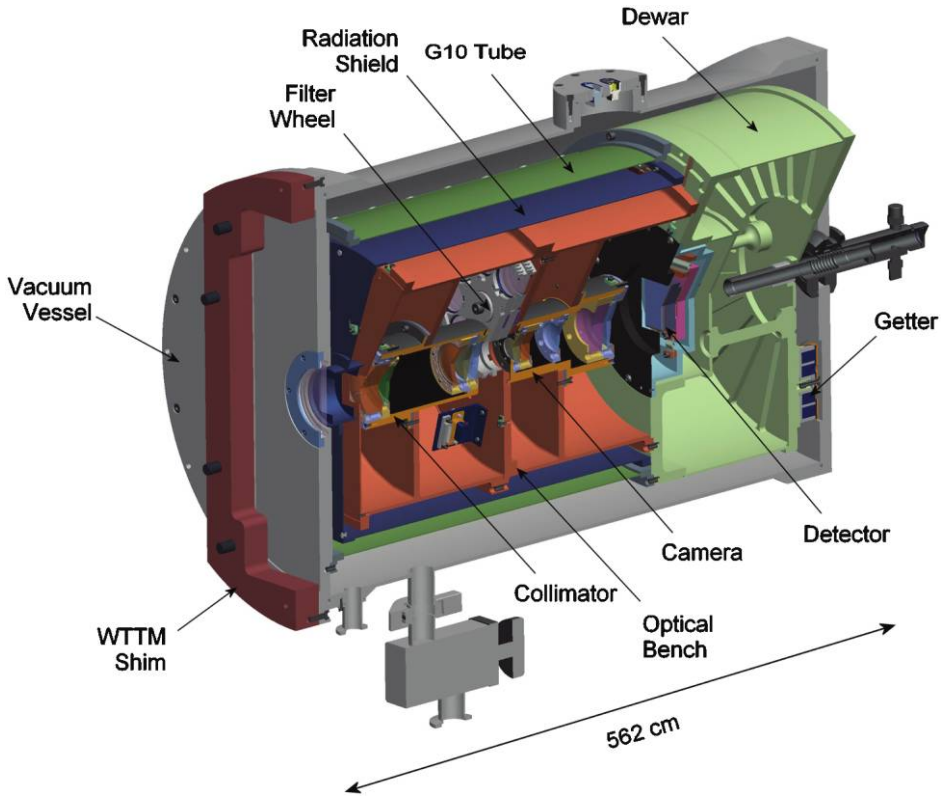


FIG. 3.—Cutaway of the WHIRC cryostat with the major subcomponents labeled. Light enters the cryostat from the left. The scale size labeled is the same as that in Figure 2.

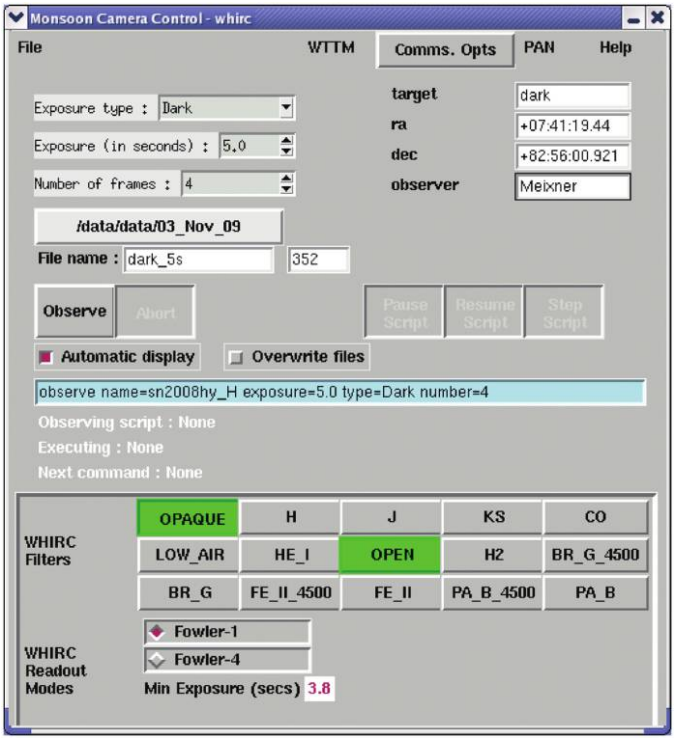


FIG. 4.—GUI used to operate WHIRC: the MONSOON Observing Platform (MOP).

### 2.4. Transient Phenomena

Observations of transient phenomena has been increasingly in demand by astronomers, and NIR observations offer some unique opportunities. Dust created in the ejecta of supernovae appears bright in the NIR. WHIRC observations in *J*, *H*, and $K_s$ can provide important constraints on the amount of dust produced by supernovae 1 yr after explosion and is detectable only with time monitoring. Dust obscures rest-frame UV flux from GRBs at high-$z$ ($z > 3$) making the NIR a more suitable avenue to follow their light curves. Rapid follow-up of GRBs is necessary, and the fact that WHIRC is permanently mounted on WIYN helps support rapid requests. NIR observations of transiting extrasolar planets can provide a measurement of the thermal emission from the planets during the secondary eclipse. Observations of transiting extrasolar planets require a high dynamic range for the light detection and the ability to support long continuous observations without interruption. FU Ori Objects are highly variable premain sequence stars undergoing mass accretion events aperiodically accompanied by up to 5 mag increases in visible brightness. These FU Ori objects have strong CO 2.3 $\mu$m band emission and monitoring of this CO feature provides direct information on their outer accretion disks (Hartmann et al. 2004).

### 2.5. Science Driven WHIRC Design Features

These science cases drove the design features of WHIRC as outlined in Table 1. The science goals make image quality the most important requirement, followed closely by point source sensitivity. Thus the image quality for WHIRC has been designed to be the highest that would be reasonably achievable with the WTTM, ~0.25″ at $K_s$. With a chosen plate scale of ~0.1″ per pixel, the FOV of WTTM is covered with a single $2048 \times 2048$ detector. The aforementioned science cases also drove the filter selection for WHIRC (see Table 1). The redshifted narrowband filters were chosen to be adjacent to the galactic or nonredshifted narrowband filters in order to provide continuum measurements for the galactic studies. Likewise, the galactic narrowband filters provide continuum measurements for the nearby galaxy studies that use the redshifted 4500 km s$^{-1}$ filters. In addition, the science drivers determined the operational procedures. The ability to dither targets is necessary to mitigate bad pixel effects on photometry. The ability to survey significant regions of the sky is very important to map nearby galaxies and large galactic star formation regions. Finally, ease of operation is an important consideration for supporting effective NIR observation programs, which often involve fast paced and repetitive exposures. All of the science goals were considered in WHIRC's design; however, the detailed design and implementation also considered constraints imposed by existing WIYN telescope interfaces and other aspects of the hardware components described in the next section.

## 3. DESIGN OVERVIEW

WHIRC has three categories of subsystems: opto-mechanical with a thermal control system; detector, mechanism, and electrical control systems; and the operations and software systems. Figure 1 outlines the components of these subsystems, where they are located at the WIYN observatory, and their communication and control paths. The WHIRC cryostat, which contains the optics, filter wheels, and the detector, all cooled with liquid

TABLE 2
WHIRC DETECTOR MEASURED PERFORMANCE

| Detector Parameter | Value |
|---|---|
| Detector type | Raytheon/VIRGO HgCdTe array |
| Size (pixels) | $2048 \times 2048$ |
| Pixel pitch ($\mu$m) | 20 |
| Wavelengths ($\mu$m) | 0.8–2.5 |
| Detector temperature (K) | $78.5 \pm 0.01$ |
| Bias voltage (V): VrstUc-Vdetcom | 0.7 |
| Gain (e$^-$ ADU$^{-1}$) | $3.3 \pm 0.2$ |
| Well depth (ADU) | 36500 |
| Well depth (e$^-$) | $120000 \pm 7000$ |
| Read noise/frame (e$^-$) Fowler-1 | $19 \pm 1$ |
| Read noise/frame (e$^-$) Fowler-4 | $11 \pm 0.6$ |
| Dark current (e$^-$ s$^{-1}$) | $0.13 \pm 0.008$ e$^-$ s$^{-1}$ |

TABLE 3
MEASURED BACKGROUND

| Filter | Background (mag arcsec$^{-2}$) |
|---|---|
| $J$ | 16.4 |
| $H$ | 14.7 |
| $K_s$ | 12.9 |

nitrogen, is mounted onto the WTTM port on the WIYN telescope. The MONSOON detector head electronics (DHE) are mounted on a nearby mounting bracket on the WIYN telescope (Fig. 2) in order to be as close as possible to the detector signal. Long ($\sim$50 ft) cables connect the controllers and power supply boxes located on the WIYN telescope level B, which is one level below the telescope floor, with the mechanisms and sensors in the WHIRC cryostat on the telescope. All but the most critical electronics boxes (i.e., MONSOON and its associated power supply) are moved to the midlevel in order to minimize the heat load near the WIYN telescope because the telescope is actively cooled to improve the dome seeing.

The WHIRC observer console and WHIRC engineering console are located at operating room level, and command of the instrument is handled through the software on these computers. In addition, the dedicated MONSOON control computer, Pixel Acquisition Node (PAN), is also located at operator room level and is connected directly to the MONSOON DHE via a fiber optic link. The console computers (linux boxes) communicate directly with the WHIRC PAN and with the controller boxes for WHIRC via the Generic WIYN Client (GWC) router on an intranet. The software interacts with the GWC router to collect all pertinent telemetry for an observation from WHIRC and the telescope system, such as position, air mass, exposure time, filter, etc.

### 3.1. Mechanical and Optical

The mechanical and optical system required a compact, low-mass instrument design, with a mass requirement of $<50$ kg, because the moment loading on the WTTM bracket must be $\sim$110 N m or less. The final design and implementation follows closely the preliminary optical and mechanical design described previously by Barkhouser et al. (2004) and is described in detail by S. A. Smee, R. H. Barkhouser, G. A. Scharfstein, M. Meixner, J. D. Orndoff, T. Miller (2010, in preparation). Figure 3 shows the cutaway of the WHIRC cryostat revealing the layout and subcomponents. The light enters through the window, passes through a five lens collimator, a filter in one of two filter wheels, a five lens camera, and onto the Raytheon VIRGO detector. A shim was inserted between WHIRC and the WTTM mounting flange in order to adjust the focus position of the WHIRC detector to match that of WTTM. The lenses are kept in place using an innovative lens cell design with roll-pin flexures. The walls of the optical bench are blackened with Z306 paint making the camera

TABLE 4
PREDICTED THROUGHPUT FROM ELEMENT ANALYSIS AND COMPARISON WITH MEASUREMENTS

| Component | Element(s) | $J$ | $H$ | $K_s$ |
|---|---|---|---|---|
| Wavelength | | 1.250 | 1.644 | 2.15 |
| Bandpass | | 0.162 | 0.300 | 0.343 |
| Atmosphere | | 0.900 | 0.950 | 0.920 |
| WIYN | 3 mirrors | $<$0.857 | $<$0.857 | $<$0.857 |
| Pickoff | | $<$0.950 | $<$0.95 | $<$0.95 |
| WTTM | 4 mirrors | $<$0.815 | $<$0.815 | $<$0.815 |
| Dichroic | | $<$0.985 | $<$0.970 | $<$0.970 |
| Window | CaF2 | 0.985 | 0.970 | 0.980 |
| Coll C1 | ZnSe | 0.960 | 0.975 | 0.970 |
| Coll C2 | ZnS | 0.965 | 0.980 | 0.970 |
| Coll C3 | ZnSe | 0.960 | 0.975 | 0.970 |
| Coll C4 | BaF2 | 0.980 | 0.975 | 0.975 |
| Coll C5 | SiO2 | 0.980 | 0.970 | 0.975 |
| Filter | | 0.913 | 0.867 | 0.877 |
| Cam L1 | BaF2 | 0.980 | 0.975 | 0.975 |
| Cam L2 | ZnSe | 0.960 | 0.975 | 0.970 |
| Cam L3 | SiO2 | 0.980 | 0.970 | 0.975 |
| Cam L4 | BaF2 | 0.980 | 0.975 | 0.975 |
| Cam L5 | SiO2 | 0.980 | 0.970 | 0.975 |
| Detector | | 0.750 | 0.900 | 0.880 |
| Total throughput | | $<$0.30 | $<$0.36 | $<$0.34 |
| WHIRC-only | | 0.510 | 0.582 | 0.575 |
| Measured total throughput | | $0.23 \pm 0.01$ | $0.27 \pm 0.02$ | $0.28 \pm 0.02$ |

TABLE 5
WHIRC Point Source Sensitivities Predictions Based on Measured Performance Characteristics

| Filter | $\lambda_0$ | $\Delta\lambda/\lambda$ | "Best" 0.25″ FWHM PSF Fitted Sensitivities 10 $\sigma$ (1 hr) Magnitudes | "Typical" 0.6″ FWHM PSF Fitted Sensitivities 10 $\sigma$ (1 hr) Magnitudes |
|---|---|---|---|---|
| $J$ | 1.25 | 0.162 | 23.6 | 22.7 |
| $H$ | 1.635 | 0.300 | 22.9 | 21.9 |
| $K_s$ | 2.15 | 0.343 | 21.1 erg s$^{-1}$ cm$^{-2}$ | 20.1 erg s$^{-1}$ cm$^{-2}$ |
| Low airglow | 1.061 | 0.0132 | $6.5 \times 10^{-17}$ | $1.56 \times 10^{-17}$ |
| He I | 1.083 | 0.0094 | $1.63 \times 10^{-16}$ | $3.91 \times 10^{-16}$ |
| Pa$\beta$ | 1.284 | 0.0158 | $1.64 \times 10^{-16}$ | $3.93 \times 10^{-16}$ |
| Pa$\beta$ (~4500 km s$^{-1}$) | 1.30 | 0.0133 | $1.46 \times 10^{-16}$ | $3.51 \times 10^{-16}$ |
| [Fe II] | 1.646 | 0.0164 | $1.85 \times 10^{-16}$ | $4.44 \times 10^{-16}$ |
| [Fe II](~4500 km s$^{-1}$) | 1.671 | 0.0162 | $1.81 \times 10^{-16}$ | $4.34 \times 10^{-16}$ |
| H2 | 2.12 | 0.0216 | $4.00 \times 10^{-16}$ | $9.61 \times 10^{-16}$ |
| Br$\gamma$ | 2.16 | 0.0215 | $4.55 \times 10^{-16}$ | $1.09 \times 10^{-15}$ |
| Br$\gamma$ (~4500 km s$^{-1}$) | 2.19 | 0.0237 | $5.17 \times 10^{-16}$ | $1.24 \times 10^{-15}$ |
| CO | 2.295 | 0.0228 | $6.98 \times 10^{-16}$ | $1.67 \times 10^{-15}$ |

very light tight. The optical bench is cooled by liquid nitrogen in the dewar and eight temperature sensors monitor the temperature of the detector, dewar, camera, collimator, and filter wheels. The detector temperature is controlled during cooldown and warm up at a rate of 1 K minute$^{-1}$ and, when cold, maintained at 78.5 K $\pm$ 10 mK using a heater and a Lakeshore 340 temperature controller. Typical cooldown times are ~7 hr and warm up times are approximately 48 hr. The filter wheels are driven using Phytron VSS-32 stepper motors controlled by AMS MAX-410 motor controllers, and their positions are measured using Hall Effect sensors on magnets and a Lakeshore 460 Gauss meter. The hold time for the cryostat meets a requirement of at least 16 hr.

### 3.2. Detector and Electrical

WHIRC houses a Raytheon VIRGO $2048 \times 2048$ pixel HgCdTe detector[10] with a 2.5 $\mu$m wavelength cutoff that is a science grade detector resulting from the lot runs for the VISTA project (e.g., McPherson et al. 2006). The VIRGO detector is controlled by the MONSOON data acquisition system developed by NOAO (e.g., Hunten et al. 2004; Buchholz & Daly 2004). The MONSOON system is split into two boxes: the DHE and the PAN. The DHE resides close to the WHIRC cryostat in order to minimize detector signal cable length. Indeed, were it not for the moment arm loading requirements, the DHE would be bolted directly to the WHIRC cryostat. The Clock and Bias board creates the voltage biases and clocks required to operate the detector. The infrared (IR) acquisition board receives the detector voltage signal on a constant current input and digitizes the signal with an analog-to-digital converter (ADC) that has a controllable sampling number for which we adopt 4, (digital average 4). The master control board routes the collection of data from the IR acquisition board to the PAN computer, located in the WIYN computer room. The pixel data are organized into an image on the PAN computer.

The VIRGO detectors were designed to be easy to read out. They require only two clocking signals, a pixel master clock (pmc) that controls the addressing sequence of the pixels, and a framestart clock that is a pulse to start the readout of a frame. Three control signals are used to set the readout modes: reduceOut selects 16 or 4 outputs, ucRstSel selects either global or rolling reset, and ucRstEn selects to reset the detector or not. Nine bias voltages are used to operate the detector. The bias voltage across the detector depends on the values of two bias voltages: Vdetcom, the detector common reference voltage, set at 1.0 V; and VrstUc, the unit cell reset voltage set at 0.3 V. The bias voltage across the detector is the difference of the two, or $-0.7$ V. The negative voltage value means it is reverse biased. Other biases are for the rail voltages for the clocks (e.g., vloReset and vhiRowEn) and the overall power for the detector.

In order to obtain the shortest possible frame time, we use the 16 output mode that divides the detector into 16 different subregions 128 active pixels wide and 2048 active pixels long. However, the total number of pixels read per subregion is $134 \times 2050$ because 6 reference pixels per row are also read, 2 before and 4 after the 128 active pixels; and 2 reference rows are read, 1 before and 1 after the 2048 active rows. One MONSOON IR acquisition board can accommodate up to 18 output lines, leaving two spare channels in our detector readout electronics.

The VIRGO is read out as follows. The detector frame rate is determined by the pmc, which is running at all times with a 14 $\mu$s per pixel clock rate. The frame start pulse is sent, and the reset enable is turned off. The pmc clocks through all pixels in the subregion in one continuous flow without the need to address individual pixels. All 16 output lines are read out simultaneously, giving a single frame time of ~3.8 s.

For the Fowler-1, or correlated double sample (CDS), readout pattern, a frame is read as described previously, the detector

[10] Module serial number VM301-48-SCA.

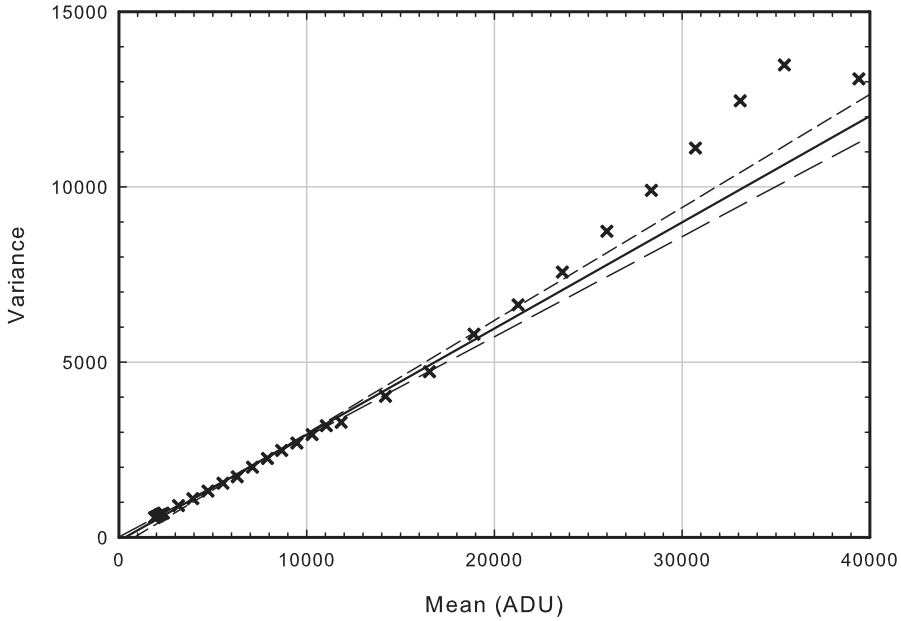


FIG. 6.—PTC for the WHIRC detector using the data from 2008 September. The linear fit to the curve indicates a gain of 3.3 $e^-$ $ADU^{-1}$ (*solid line*), and the two neighboring lines show the uncertainty in the fit of $\pm 0.2$.

accumulates charge for the length of the exposure time specified by the user, and then a second frame is read. Subtraction of the second frame from the first frame is performed in the PAN and stored as a FITS (flexible image transport system) file. The minimum possible exposure time in Fowler-1 is the readout time of 3.8 s, but astronomical observations typically use 4 or 5 s as

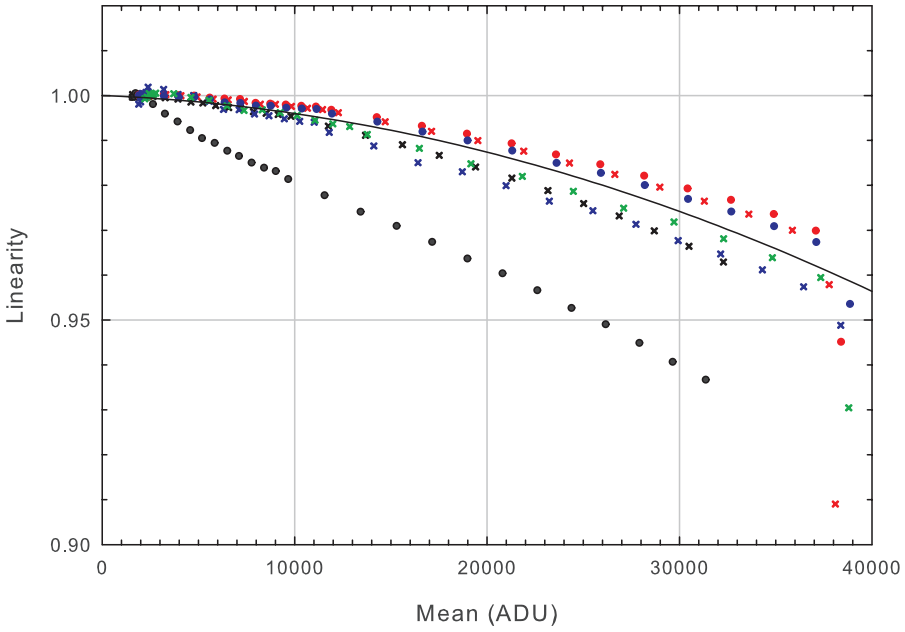


FIG. 7.—Plot of the linearity as a function of mean signal (ADU) for the bias value of 0.7 V. The linearity is defined as the signal flux (ADU per second) normalized to the average signal flux value at 5.0 s integration time. See the electronic edition of the PASP for a color version of this figure.

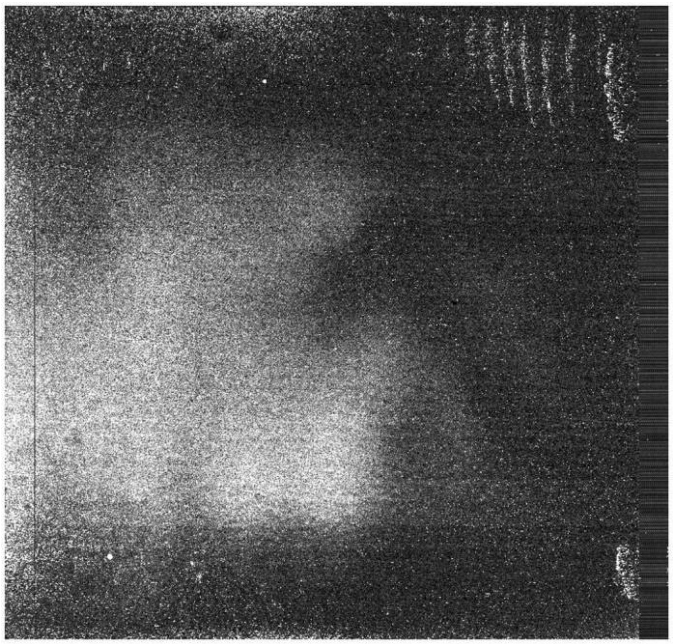

FIG. 8.—Dark image with 100 s integration. The "palm print" structure in the dark image subtracts out like sky emission in the data reduction procedure. The reference pixels are located at the top and right-hand side, as they appear in the raw data.

the minimum. This Fowler-1 mode has been used for most testing because it is quick and is used for broad-band imaging of most sources and for the brightest sources. In order to improve the noise for faint object broadband imaging and for narrow-band imaging, we also developed a Fowler-4 readout pattern (Fowler and Gatley 1990). In Fowler-4 mode, four consecutive frames are read out and summed in the PAN memory. The detector then accumulates charge for the length of the exposure time. Finally, four consecutive frames are read again and subtracted from the frames in PAN memory. There is no division by 4 in the PAN memory to avoid digitizing effects in the integer data output. The minimum integration time is 15.2 s.

When the detector is not exposing on an object, it is in idle mode during which the detector is continuously reset using the rolling reset mode. The VIRGO detector was tested for both global reset mode, which resets all the pixels at once, and the rolling reset mode, which resets the detector rapidly as it is clocked. We decided on the rolling reset mode because it gave a more consistent reset level value and deeper well depth.

TABLE 6

HUNT ET AL. AND 2MASS STANDARDS IN NGC 7790

| Star, AS 40-# | | $J$ | $H$ | $K_s$ |
|---|---|---|---|---|
| 0 ..... | Hunt | 11.051 | 10.408 | 10.240 |
| | 2MASS | 11.010 | 10.336 | 10.229 |
| 1 ..... | Hunt | 11.900 | 11.097 | 10.861 |
| | 2MASS | 11.919 | 11.137 | 10.884 |
| 2 ..... | Hunt | 11.477 | 10.569 | 10.314 |
| | 2MASS | 11.468 | 10.504 | 10.313 |
| 3 ..... | Hunt | 10.578 | 9.966 | 9.785 |
| | 2MASS | 10.602 | 9.943 | 9.787 |
| 4 ..... | Hunt | 10.356 | 9.695 | 9.516 |
| | 2MASS | 10.337 | 9.653 | 9.500 |
| 5 ..... | Hunt | 9.488 | 9.418 | 9.405 |
| | 2MASS | 9.496 | 9.432 | 9.447 |

### 3.3. Operational and Software Interface

Three software interfaces were developed in order to make observations with WHIRC easy and efficient. A WHIRC engineering graphical user interface (GUI) is used to monitor temperatures, to manage the detector biasing procedures, and to monitor the filter wheel positions. The Lakeshore controller automatically controls the temperature of the detector and ensures controlled cooldown and warm up of WHIRC. The WHIRC engineering GUI provides a way to monitor the detector temperature and to initiate the cooldown and warm up procedures. The WIYN observatory staff bias the detector only when it is appropriately cold. Software safeguards are used to automatically debias the detector should the temperatures rise above a critical threshold of ~90 K. The WHIRC engineering GUI provides low-level monitoring of the filter wheel positions and is used to debug problems and reset the filter wheel home position.

The MONSOON Observing Platform (MOP, Fig. 4) is the primary user interface for operation of WHIRC. The observer can select filter position, readout modes (Fowler-1 or Fowler-4), exposure times, number of sequential exposures, and simple dither patterns from this interface. The user can also enter target names, object types, and root filenames, to which the interface automatically appends an incrementing extension. The MOP is also used to initiate scripted series of exposures such as complex dithering and mosaicking patterns generated by the WHIRC Observation Manager and Planner (WHOMP, Fig. 5). With the WHOMP, one can create a custom mapping and dither pattern for an object; this generated pattern can be overlaid on a Digitized Sky Survey (DSS) image of the field in the DS9 image display. The WHOMP generated dither and mapping pattern is saved as a scripting file that is selectable by the observer from the MOP.

The WHIRC control software has generally been reliable in normal observing operation. Because of the complex communications architecture (Fig. 1), some failures are inevitable, but many appear to result from interfacing issues with the WIYN client router. We have established a checklist for proper initialization of the system components and made some modifications to the MOP to prevent inadvertent commands while data are being taken, both of which have improved system reliability. The WHIRC software was able to sustain one continuous 8 hr observation of a transiting extrasolar planet without

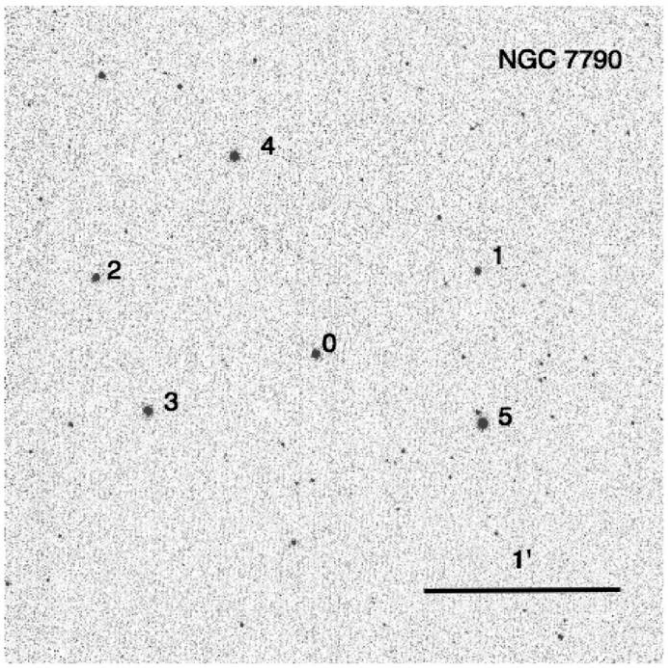


FIG. 9.—NGC 7790 imaged at *H* band by WHIRC. The standards from AS-40 (Hunt et al. 1998) standard are labeled by their number (see Table 6) and cover the WHIRC FOV well. Star 5 was resolved into a double by WHIRC, where as Hunt et al. and 2MASS catalogs list only one star with the combined flux from both stars.

crashing in 2008 November. We have received positive feedback from the shared risk users that the interface is relatively straightforward to use and is well documented in the user's guide (Joyce et al. 2009).

## 4. WHIRC DETECTOR AND INSTRUMENT SENSITIVITY

The performance characteristics of WHIRC are detailed in Tables 1–5. The resulting sensitivity of an instrument depends on the detector characteristics (Table 2), the background signal level (Table 3), and the throughput of its optical pathway (Table 4). The sensitivity values summarized in Table 5 are estimates based on a model of the WHIRC + WIYN + sky system using the measured performance of the detector and measured throughputs. In this section, we describe the measured on-telescope performance of the detector, throughput of WHIRC, background emission, and resulting instrument sensitivity.

### 4.1. WHIRC's Raytheon VIRGO 2048 × 2048 Detector Characteristics

In this subsection, we describe the measurements or reasoning behind the WHIRC detector characteristics summarized in Table 2. As with any IR detector, the performance of the WHIRC detector depends on how it is biased. The effective bias across the detector is the difference of VrstUc and Vdetcom; because the detector is reverse biased, this is a negative value but for convenience we use the absolute value in the text. The recommended bias setting procedure from Raytheon is to keep Vdetcom at 1.0 V and to change the bias by setting VrstUc between 0 and 1.0 V (Raytheon VIRGO user's guide, Raytheon Vision Systems 2004). We tested detector biases of 0.5, 0.7, 0.8, and 1.0 V (Joyce 2008a). We adopted 0.7 V for the WHIRC detector bias because it provides the best balance of detector characteristics such as linearity, well depth, hot pixels, and read noise.

#### *4.1.1 Photon Transfer Curve (PTC)*

We measured the PTC for WHIRC on 2008 September 17 (UT) using the $H_2$ filter and dome flat illumination. Different intensity levels were measured by increasing the integration time, and five measurements were made at each integration time to improve statistics. A set of three short exposures (5 s) were taken in between each integration time in order to verify that the dome lamp light was stable throughout the time; this was confirmed by an analysis of these images. We created a PTC by calculating the mean and variance of the array, excluding the outer 100 pixel perimeter, for each of the different intensity levels (exposure times). In Figure 6, we plot the variance versus the mean flux value for this PTC data set. At mean count levels above $\sim 15,000$ ADU, the PTC data appear to be affected by a short lived detector persistence that causes irregularities in the measured variance. We fit a line to the data with mean values less than $\sim 15,000$ and derive a gain of $3.3 \pm 0.2$ $e^-$ $ADU^{-1}$ (Fig. 6). The PTC also reveals the full well at which detector saturation is reached to be 36,500 ADU or $120,000 \pm 7000$ $e^-$. The corresponding saturation magnitude in the shortest exposure is approximately 10–11 in the broadband filters but depends on seeing conditions.

All IR detectors are inherently nonlinear, and the strategy is to correct the nonlinearity as one of the initial data processing steps. We defined the linearity as the signal flux (ADU per second) normalized to the average value at 5.0 s integration time (Fig. 7). The linearity data sample from six of the seven subregions shown in Figure 8 were fit with a simple quadratic equation of the form $y = a + bx + cx^2$, where $y$ is the linearity, $x$ is the mean counts value in ADU, and $a$, $b$, and $c$ are the best-fit coefficients. Fitting the data with mean count values below 36,000 ADU gives coefficients of $a = 1.000$, $b = -3.62 \times 10^{-7}$, and $c = -1.839 \times 10^{-11}$. By inverting this function, one can derive a linearity correction function so that the corrected signal, $S'$, is related to the raw signal, $S$, by $S' = S(A + B \times S + C \times S^2)$, where $A = 1.000$, $B = 1.29 \times 10^{-7}$, and $C = 2.506 \times 10^{-11}$. Converting to the units used by the IRAF task, irlincor, which is specifically designed to carry out this correction, the nonlinearity coefficients are $A_{\rm ir} = 1.000$, $B_{\rm ir} = 0.004227$, and $C_{\rm ir} = 0.02691$.

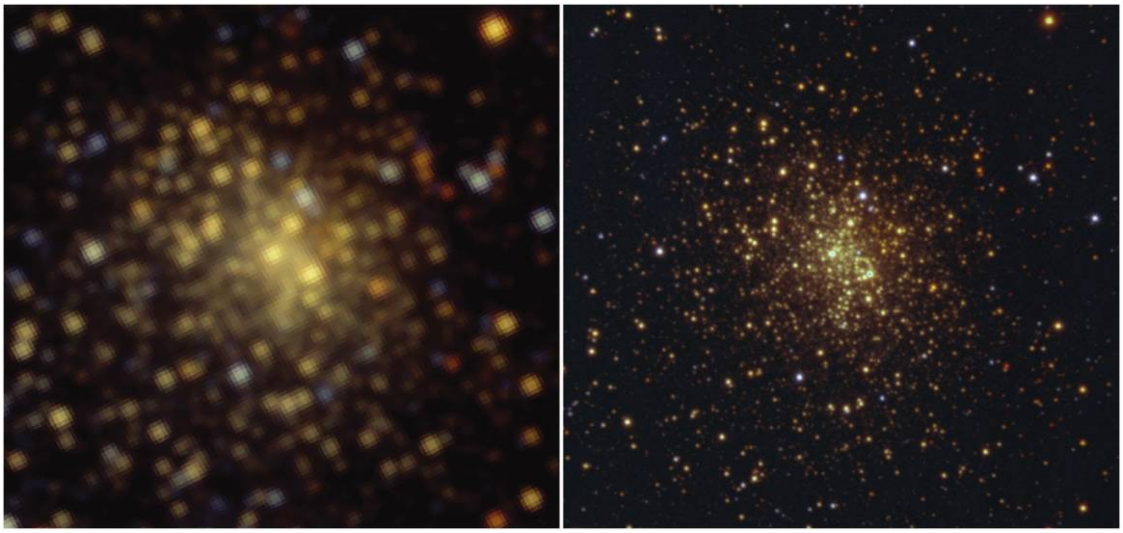

FIG. 10.—Comparison of a false-color 2MASS image (*left*) of the GLIMPSE GC-1 Galactic Plane Globular Cluster and a WHIRC image (*right*) of the same field. The colors are $J$, $H$, and $K_s$ (*represented by blue, green, and red, respectively*) for both images. (*Image credit: Matt Povich, University of Wisconsin.*)

#### *4.1.2. Dark Current*

We measured the dark current for WHIRC in 2008 September by moving the filter wheel to the opaque position, which is a blackened metal cold piece. We measured 1–3 dark images at exposure times of 100, 1000, and 2000 s using Fowler-1. From these three measurements we derive dark current ranges from 0.026 to $0.026$–$0.16$ ADU $s^{-1}$ with a median value of $0.039$ ADU $s^{-1}$. Using our derived gain of $3.3 \pm 0.2$ $e^-$ $ADU^{-1}$, we determine the dark current to have a median value of $0.13 \pm 0.01$ $e^-$ $s^{-1}$. Our dark current measurement inside of WHIRC is comparable to that measured by Raytheon for this detector when it was sealed tightly against light using their test setup. Thus, our dark current measurement is a testament that the cryostat is very light tight. Figure 8 shows the dark frame from 100 s integration with the reference pixels reorganized to the right and top of the detector in a frame as it comes in raw form from the WHIRC PAN. Spatial structure in the dark frame called the "palm print" is stable and subtracts out like sky background during the data reduction process.

#### *4.1.3. Read Noise*

Noise performance for WHIRC is dominated by readout noise at short integration times and background sky emission at longer integrations. We measured the read noise on 2008 September 16 with the filter wheel in the opaque position. A series of 10 short darks were taken in both the Fowler-1 (4 s exposure time) and Fowler-4 (16 s exposure time) detector readout modes. The statistics were measured across the whole detector by using IRAF task, imcombine, to make median and sigma images of the 10 short dark measurements. The reported read noise uses the measured gain of $3.3$ $e^-$ $ADU^{-1}$ and is normalized to a single frame by dividing these values by $\sqrt{2}$. The Fowler-1 readout mode has a readout noise of 5.8 ADU or $19 \pm 1.2$ $e^{-1}$. The Fowler-4 readout mode has a read noise of 3.2 ADU or $11 \pm 0.6$ $e^{-1}$. The Fowler-4 detector readout reduces the read noise by a factor of 2, as expected. The read noise is measured every night of WHIRC observing as part of the WIYN performance monitoring program.

### 4.2. Background, Throughput, and Resulting WHIRC Sensitivity Models

#### *4.2.1. Background Measurements*

We measured the backgrounds of the WHIRC + WIYN + sky emission by calibrating the uniform background emission during a long exposure of a standard star in spring 2008. These measurements are reported in Table 3. The sky emission dominates at *J* and *H* band. The telescope, especially the last dichroic before the WHIRC instrument, dominates the background emission measured at $K_s$. The sky background level during the summer is higher for bandpasses where thermal effects limit performance, e.g., filters falling in the *K* band.

#### *4.2.2. Throughput*

The predicted throughputs for each of the WHIRC broadband filters are listed by element in Table 4. Typical band-wide atmospheric transmission values were assumed for the three filters ($J = 0.90$, $H = 0.95$, $K_s = 0.92$; R. F. Green, private communication[11]). The WIYN telescope and the WTTM present a

[11] See, e.g., ftp://ftp.noao.edu/catalogs/atmospheric_transmission/.

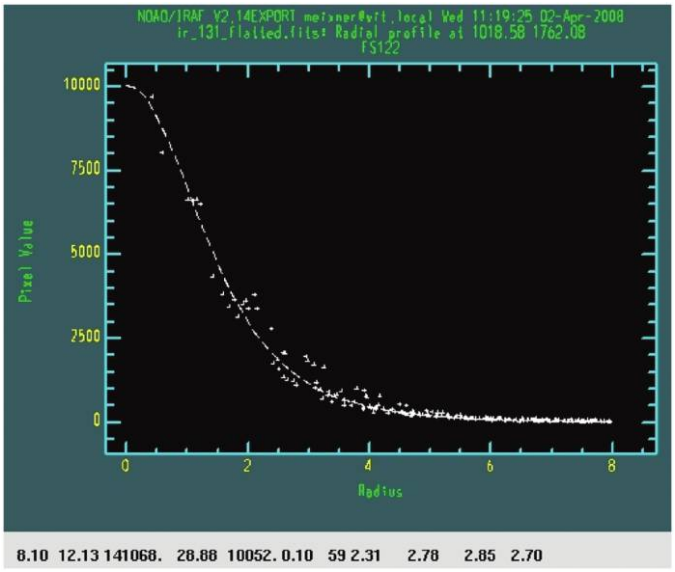


FIG. 11.—The radial fit to the PSF of a star in the FS 122 field imaged in $H$ band on 2008 January 20. The radius, in units of pixels, translates to an FWHM$\sim 0.28''$ without any active correction.

number of surfaces for which reflectance values of 0.95 have been assumed for each and multiplied by the number of surfaces. We consider these WIYN and WTTM values to be upper limits, because they do not fully include the effects of degradation or dust scattering on the surfaces. The values for the dichroic are the vendor-measured values; however, because this element is external to the cryostat, it can gather dust and degrade in performance and should be considered an upper limit. In addition, the absolute atmospheric transmission is difficult to determine, particularly any scattering loss due to aerosols. Vendor-supplied values were used for the transmission of WHIRC optics including the window, collimator, filters, and camera, as well as the detector QE in each band. The total throughput is calculated by multiplying all the throughput values in Table 4. The WHIRC-only throughput values include only those components contained in the WHIRC instrument from the window through the detector. Comparison of the measured throughput, described subsequently, should be made with the total throughput analysis, which are upper limit values of 0.30, 0.36, and 0.34 for the $J$, $H$, and $K_s$ bands, respectively.

The WHIRC throughput for each filter was measured with data collected on 2008 September 15 (Table 4). The Hunt et al. (1998) standard field NGC 7790 contains a cluster of six standards, AS 40-0 to AS 40-5 (Table 6 and Fig. 9), that were imaged in all three broadband filters $J$, $H$, and $K_s$. The average seeing was $\sim 0.7''$ in the $K_s$ band. The standard star field was observed with a five-point dither pattern on the detector. The images were processed using the WHIRC wprep.cl script that corrects for the nonlinearity using irlincor and strips off the reference columns and rows. We created a sky image by combining all five images using median filtering in the IRAF task, imcombine, and subtracted the resultant sky from each image. We then flat-fielded each image using dome flats that were corrected for the pupil ghost. The IRAF task phot was used to perform aperture photometry (with sky subtraction) on each of the standard star images. We used an aperture radius of $7''$, a sky radius of $8''$, and a sky annulus of $1''$. The aperture was large enough to include the AS 40-5 double, which WHIRC resolved but was included as a single star in the Hunt et al. (1998) photometry study. We measured the total counts (ADUs) for each of the siz stars. As there were five dither positions, five measurements for each of the six stars were obtained, except for star AS 40-2,

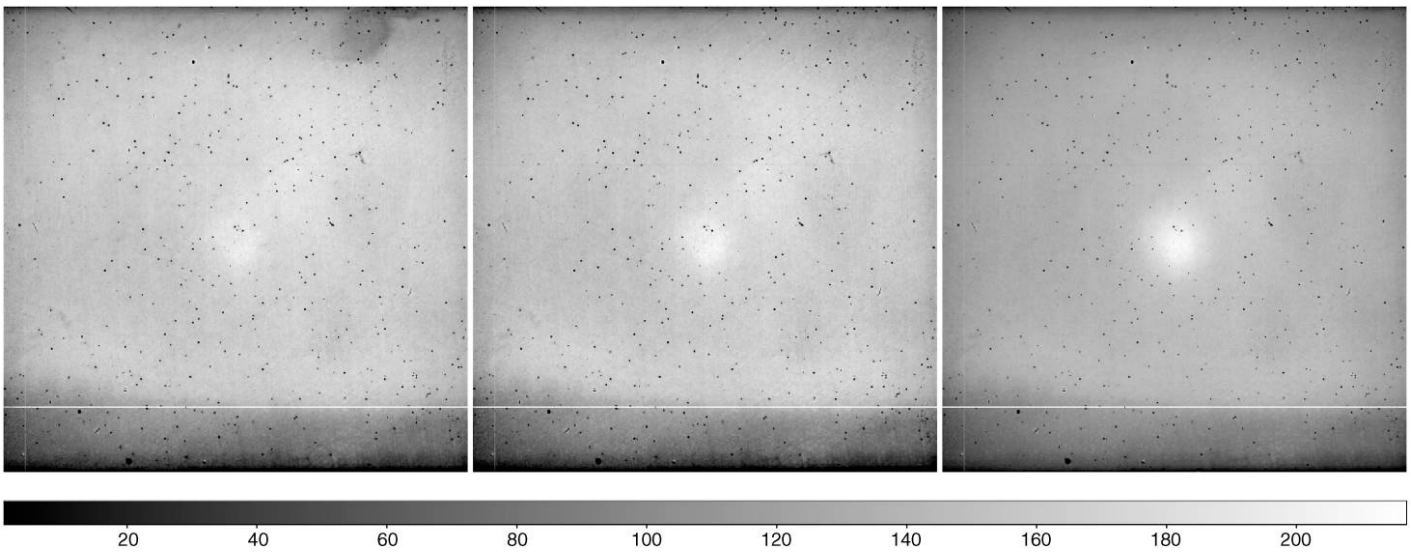


FIG. 12.—WHIRC dome flats from left to right in the bands: $J$, $H$, and $K_s$; see text.

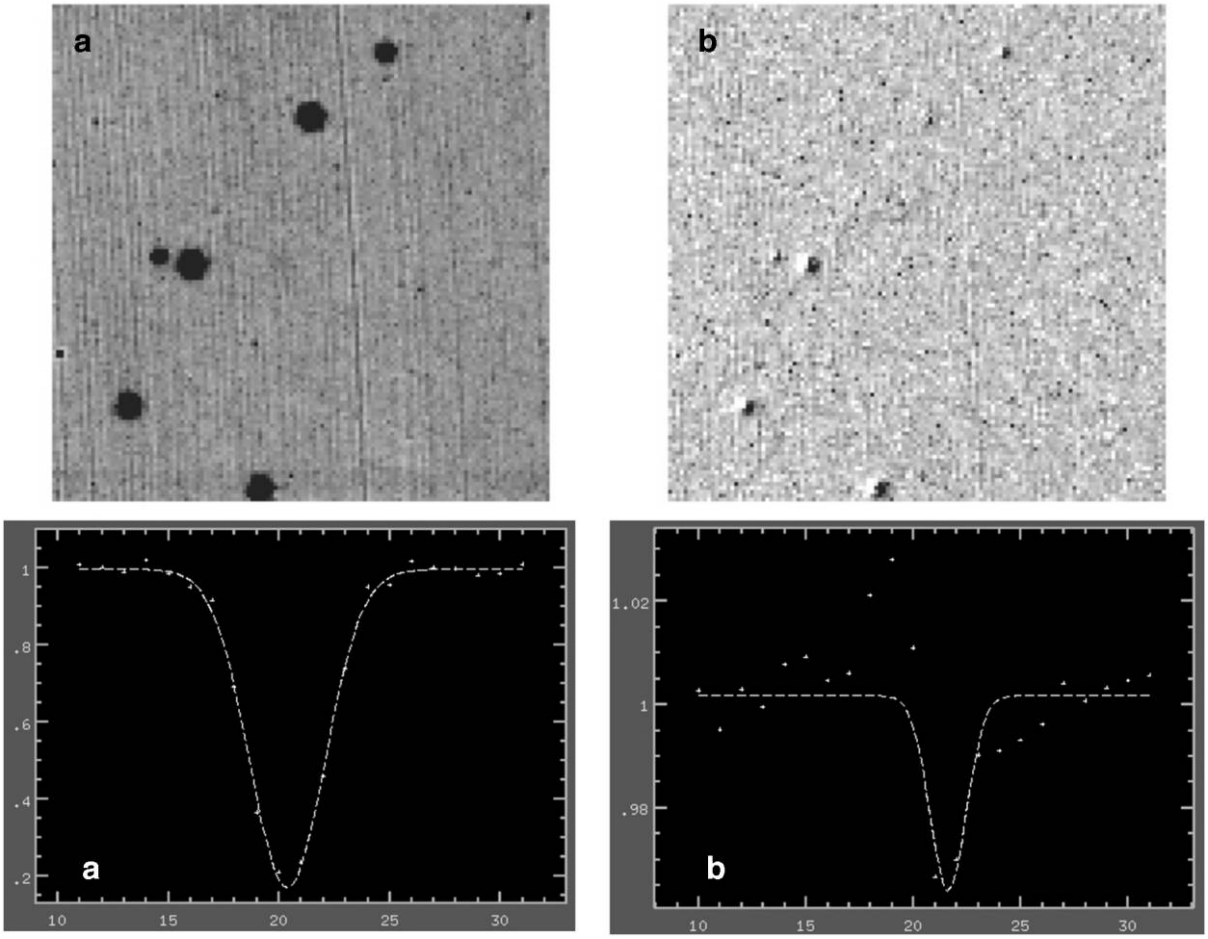


FIG. 13.—(*a*) 128 × 128 subimage of an *H*-band dome flat, showing the normal "tree-ring" structure and the circular, apparently dead features (*top*). Line plot through one of the spots shows that the features are not dead pixels but regions of reduced responsivity (*bottom*). (*b*) Ratio of two separate flat fields taken 5 months apart shows that the features are quite stable over long periods (*top*). Line plot through a ratioed spot demonstrates the stability to within a few percent (*bottom*).

which fell off the array for one dither position leaving four measurements. An average signal for each filter was computed from the five (four) individual photometric measurements. The average signals were converted to a count rate in (photo)electrons per second based on the exposure times and measured gain of $3.3 \pm 0.2$ $e^-$ $ADU^{-1}$. The expected standard star count rate was also computed for each band based on its published magnitude. The measured (photo)electrons per second rate divided by the photon count rate derived from the known magnitudes in each band gives the throughput. The measured throughputs are an average of the six stars and the standard deviations of the six measurements are on the order of 0.008. The errors on the measured throughputs are determined by the uncertainty in the detector gain, which is larger than the uncertainty in the photometry.

A comparison between the predicted and measured throughputs is presented in Table 4. The measured throughputs appear lower than those predicted by the element analysis. However, we note that the predicted throughputs are upper limits. Overall, our measured values are consistent with the predictions, but we suggest that any sensitivity estimator use the measured throughput values for best accuracy. For example, if we were to reduce the three WIYN mirror reflectivities to 0.9 (from 0.95) the element analysis reconciles with the measured throughput. For the purposes of the sensitivity calculations presented in this article, we adopt 0.9 for the reflectivity of the WIYN mirrors; however, we note that the lower throughput could be caused by any of the elements or the atmosphere.

#### *4.2.3. Sensitivity Estimates*

In Table 5, we provide our estimates for the best possible point source, 0.25″ FWHM PSF (point spread function), and more typical point source, 0. 6″ FWHM PSF, sensitivities. These estimates are calculated from a radiometric model of WHIRC + WIYN + atmosphere over Kitt Peak and include the emission as well as the throughput of these elements. For this model, we

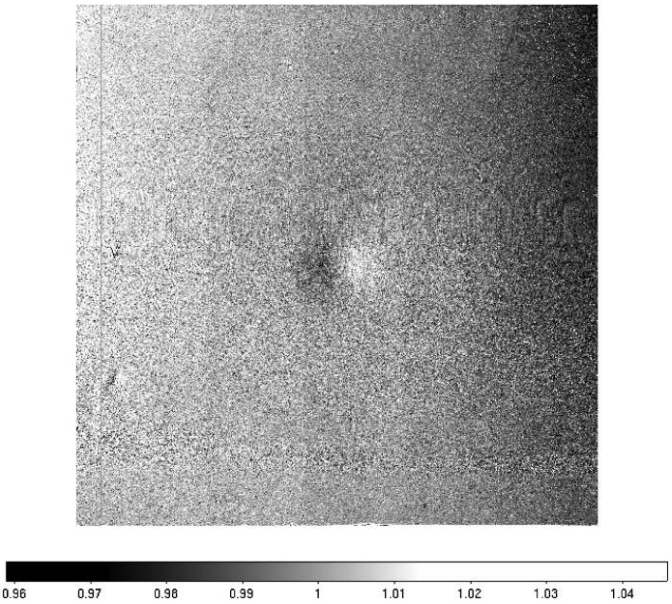


FIG. 14.—Image of the ratio of a $K_s$ dome flat from 2008 July 17 to one obtained on 2008 April 15. Deviations from unity are generally less than 1%. This illustrates the long-term stability of the instrument flat-fielding.

use the throughput values from Table 4 but degrade the WIYN telescope reflectivity so that this model is more in line with the measured throughput (see § 4.2.2). The WIYN telescope and WTTM background emission properties are based on a temperature of 300 K, emissivity of the optical elements ($=1-$ transmission), and blackbody radiation. Emission, particularly from the telescope, is a significant source of noise at the longer wavelength (*K* band) filters. We include the measured noise performance of the WHIRC detector. We use the read noise values corresponding to the detector readout pattern appropriate for the filter selections: Fowler-1 for the broad bands and Fowler-4 for the narrow bands.

The sensitivity numbers are for a point source sensitivity using a PSF fitting photometry approach (as opposed to aperture photometry) because less sky is included and sensitivity is maximized. For the "best" sensitivity estimates, we assumed a PSF with a Gaussian shape and an FWHM of 0.25″, which is the anticipated PSF size for WTTM + WHIRC in $K_s$ band imaging under good seeing conditions. However, without the WTTM WHIRC typically has an FWHM of ~0.6″, and thus we include a second column noting these more typical sensitivities.

The model sensitivity for WHIRC was verified in 2008 July by visiting Yale observers at $J$-band during a 1.0 hr long integration of a deep field that contained several 2MASS sources. Estimates from these measurements indicate a $10\sigma$ sensitivity limit of $J \sim 21.4$ mag in 1 hr on-source time using a 1.6″ aperture for aperture photometry. This measurement is consistent with the sensitivity model prediction of 21.1 mag using a 1.6″ radius aperture.

## 5. WHIRC IMAGING AND PHOTOMETRIC PERFORMANCE

In this section, we discuss WHIRC's performance as an imaging and photometric camera including its achieved image quality, measured plate scale, and flat-field characteristics. We show that ghosts do not affect any source within WHIRC's dynamic range. We demonstrate its photometric quality is better than ~0.02 mag. We briefly discuss WHIRC + WTTM performance.

### 5.1. Image Quality

WHIRC's image quality is its biggest selling point for both imaging and high sensitivity point source detection and photometry. We verified the image quality in three ways. The pinhole tests used for alignment on the telescope demonstrated that the combined optics of WTTM and WHIRC had an FWHM of $2.0 \pm 0.1$ pixels or 0.2″. The pinhole test provided a grid of pinholes across the WHIRC FOV revealing some variation in structure due largely to the WTTM optics that introduces a slight astigmatism and distortion.

Images of clusters, such as the GLIMPSE globular cluster shown in Figure 10, demonstrate that onsky image performance

TABLE 7
PHOTOMETRIC QUALITY TEST BASED ON FIVE STANDARDS IN NGC 7790 PER DITHER POSITION

| | $J$ | | $H$ | | $K$ | | Pa$\beta$ | | Fe II | | Br$\gamma$ | |
|---|---|---|---|---|---|---|---|---|---|---|---|---|
| Dither Position | No Flat | Flat | No Flat | Flat | No Flat | Flat | No Flat | Flat | No Flat | Flat | No Flat | Flat |
| 1 ..... | 0.080 | 0.011 | 0.074 | 0.012 | 0.070 | 0.005 | 0.102 | 0.025 | 0.098 | 0.009 | 0.107 | 0.009 |
| 2 ..... | 0.023 | 0.013 | 0.017 | 0.017 | 0.025 | 0.031 | 0.331 | 0.016 | 0.048 | 0.008 | 0.052 | 0.009 |
| 3 ..... | 0.026 | 0.026 | 0.021 | 0.024 | 0.039 | 0.032 | 0.030 | 0.028 | 0.031 | 0.022 | 0.021 | 0.013 |
| 4 ..... | 0.096 | 0.014 | 0.081 | 0.008 | 0.073 | 0.005 | 0.104 | 0.016 | 0.103 | 0.012 | 0.094 | 0.042 |
| 5 ..... | 0.029 | 0.010 | 0.029 | 0.016 | 0.025 | 0.010 | 0.050 | 0.013 | 0.052 | 0.010 | 0.042 | 0.026 |
| 6 ..... | 0.049 | 0.026 | 0.035 | 0.026 | 0.044 | 0.021 | 0.038 | 0.024 | 0.034 | 0.022 | 0.022 | 0.013 |
| 7 ..... | 0.105 | 0.014 | 0.088 | 0.017 | 0.086 | 0.012 | 0.120 | 0.020 | 0.095 | 0.014 | 0.116 | 0.029 |
| 8 ..... | 0.023 | 0.017 | 0.073 | 0.022 | 0.018 | 0.020 | 0.057 | 0.016 | 0.061 | 0.019 | 0.067 | 0.009 |
| 9 ..... | 0.034 | 0.024 | 0.035 | 0.024 | 0.031 | 0.031 | 0.031 | 0.027 | 0.027 | 0.022 | 0.021 | 0.017 |
| Average ..... | 0.052 | 0.017 | 0.050 | 0.018 | 0.046 | 0.018 | 0.096 | 0.020 | 0.061 | 0.015 | 0.060 | 0.019 |

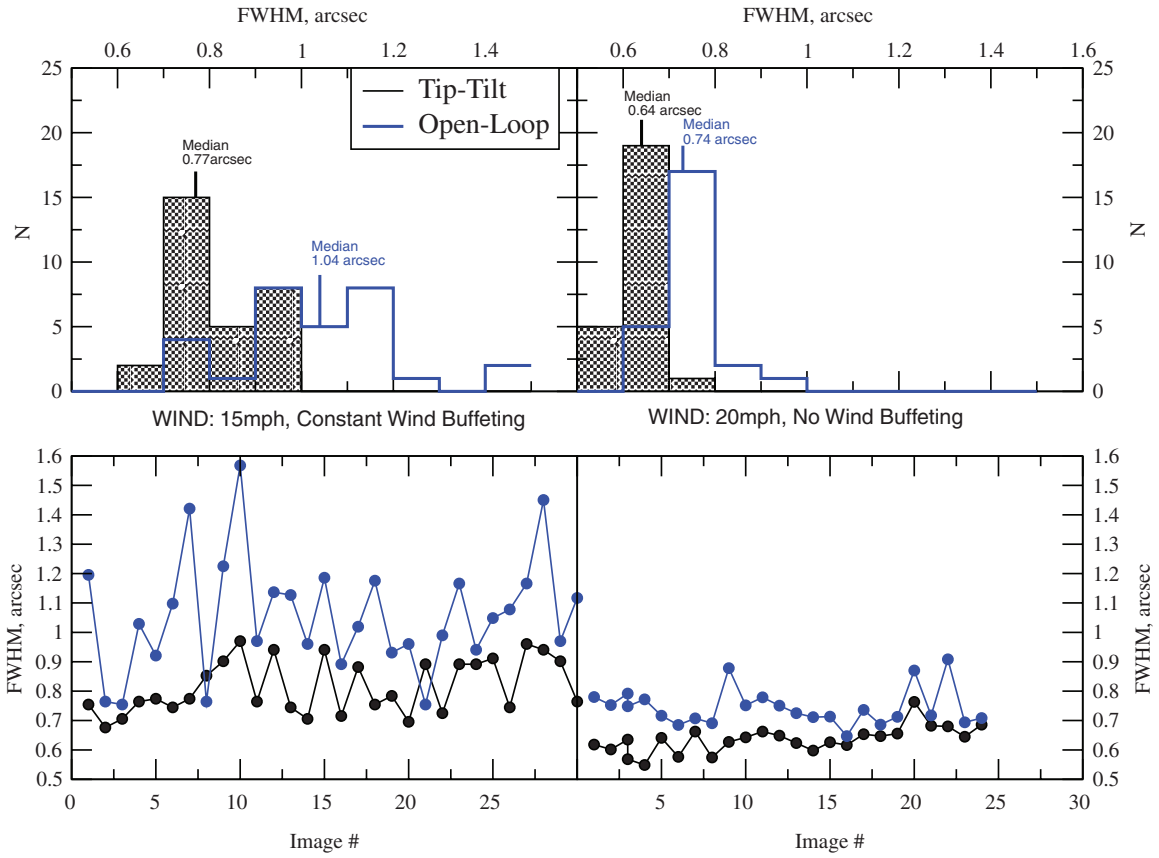


FIG. 15.—Results of two tests to measure the FWHM improvements from turning on WTTM correction, using 10 s exposures in the $H$ band. The results are consistent with the predicted improvements of 0.1–0.15″ and even more significant when wind buffeting is a factor. (*Courtesy of C. Corson and H. Schweiker.*)

has been as good as ~0.6″ FWHM across the field under typical observing conditions. This image demonstrates the dramatic improvement of WHIRC's image quality over the public access 2MASS data. The 2MASS images have on source integration time of ~8 s band$^{-1}$. The WHIRC image is a combination of $4 \times 16$ s dithers per band (plus an additional $4 \times 32$ s dither at $J$-band) from data taken on 2007 September 26 and 27. Finally, Figure 11 shows the radial profile of a standard star, FS 122, with an ~0.28″ FWHM measured on 2008 January 20. Thus excellent image quality is possible without active correction on occasion, and WHIRC will not be limiting the typical performance of the WTTM + WHIRC system.

### 5.2. Plate Scale

The WHIRC optical system was designed to meet a plate scale requirement of ~1″ per pixel. The open cluster NGC 6791 was imaged using WHIRC in 2007 August for the purpose of verifying this requirement. The coordinates and NIR photometry of the stars in NGC 6791 were measured previously using FLAMINGOS on the Mayall 4 m Telescope at Kitt Peak by Carney et al. (2005). A three star fit using the IDL astro library routine STARAST resulted in a plate scale of 0.098″ pixel$^{-1}$. However, the known distortion introduced by the WTTM optics results in a slight asymmetry in the pixel scale. A later measurement of the plate scale on globular cluster M13 in $J$, $H$, and $K_s$ used 22 isolated 2MASS stars and the IRAF routine ccmap. The plate scales in the two dimensions were determined to be 0.099″ and 0.10″ pixel$^{-1}$, in agreement with the prior result but now defining the asymmetry in the pixel scale. In both measurements, there is no significant color dependence of this result in the three filters verifying the design requirement that filter changes would not induce effects on the image quality, plate scale, or focus.

### 5.3. Flat-Field Characteristics

Dome flat fields for WHIRC are made with the telescope pointing at the WIYN white screen by taking ~11 exposures with the flat-field lamp on followed by ~11 exposures with the lamp off. Figure 12 shows the dome flats for $J$, $H$, and $K_s$. The individual flat-field images are stripped of reference pixels and corrected for nonlinearity. The lamp-on and lamp-off frames are combined using a median algorithm, and the resultant lamp-off image is subtracted from the lamp-on image.

TABLE 8
COMPARISON WITH OTHER NIR CAMERAS ON 3–4 M CLASS TELESCOPES

| Telescope Instrument (hemisphere) | Year | Array Format $\lambda$ ($\mu$m) | Pixel Scale (arcseconds pixel$^{-1}$) | Field of View ($''$) | $\Omega$ | $10\sigma$ 1 minute $J$, $H$, $K_s$ | Number of Filters |
|---|---|---|---|---|---|---|---|
| (1) | (2) | (3) | (4) | (5) | (6) | (7) | (8) |
| KPNO/CTIO 4 m NEWFIRM (north/south) | 2008 | InSb, 4K × 4K 0.9–2.4 | 0.40 | 1656 | $4 \times 10^6$ | 19.8, 19.0, 18.0 | 13 |
| SOAR 4.2 m SPARTAN (southern) | 2009 | HgCdTe, 4K × 4K 0.9–2.5 | 0.04, 0.07 | 180, 300 | $2 \times 10^6$ | — | 15 |
| WIYN 3.5 m WHIRC (northern) | 2008 | HgCdTe, 2048 0.9–2.5 | 0.1 | 205 | $10^6$ | 18.7, 18.0, 16.3 | 13 |
| KPNO 4 m FLAMINGOS (north/south) | 2000 | HgCdTe, 2048, 0.9–2.5 | 0.3 | 600 | $6 \times 10^5$ | 18.8, 18.0, 17.6 | 4 |
| ISPI CTIO 4 m (south) | 2002 | HgCdTe, 2048 0.9–2.5 | 0.3 | 600 | $6 \times 10^5$ | 18.1, 17.5, 17.0 | 12 |
| IRTF 3 m NSFCAM2 (north) | 2006 | HgCdTe, 2048, 0.9–5 | 0.04 | 80 | $10^5$ | 17.5, 17.6, 16.5 | 19 |

Finally, a normalized flat field is made by dividing the lamp-on-off image by its mean of the ADU counts, excluding the very center $\sim 500 \times 500$ pixel region where the pupil ghost lies (see § 5.3.1). Very small and negative values in the normalized flat are replaced with the number 1 to avoid creating artificially large pixel values in the flat-fielded image. These flat fields have a mean of $\sim 0.95$, and their standard deviations are 0.0919, 0.0832, and 0.0827 for the $J$, $H$, and $K_s$ bands. The approximate range (low and high) values are 0.8–1.02, 0.8–1.03, and 0.7–1.02 for $J$, $H$, and $K_s$, respectively. For all wavelengths, the sensitivity at the bottom eighth of the detector is significantly lower than the remainder of the array. The white line that lies at the top of this insensitive portion is a defective row. At the top part of the detector in the $J$ band dome flat there is a dark thumb print of lower sensitivity, which is possibly a defect in the antireflection coating on the detector. A bright pupil ghost at the center of the detector, which is not a sensitivity variation, and black dimples across the detector, which are sensitivity variations, are common to all flat fields and are described subsequently.

#### *5.3.1 Pupil Ghost*

Dome flats reveal a false intensity increase at the center of the detector due to a known pupil ghost in the system. Pupil ghosts are often seen in on-axis refractive imaging systems, but the effect in WHIRC is more pronounced, particularly in the *K* band, because of the large number of ambient temperature optics in the WTTM train. The lamp-on–lamp-off technique for obtaining dome flats, which is commonly employed with IR imagers, is particularly suitable for WHIRC because this technique eliminates those components of the pupil ghost that are due to thermal emission from the warm optics. However, the remaining pupil ghost from the dome flat will still require correction and has recently been calibrated for removal using a low-frequency flat that appears to work for all wavelengths.

#### *5.3.2. Dimples*

A typical flat-field image shows numerous circular features that appear to be array defects (Fig. 13a). The cause of these features is unknown. However, it is important to realize that these are not dead pixels but regions of depressed sensitivity that still respond linearly to radiation; as a result, they can be largely corrected by flat-fielding (Fig. 13b). The system sensitivity within these regions is, of course, reduced. The measured flux from a star that falls on one of these regions will be significantly reduced in unflattened images but relatively unaffected in the flattened images.

#### *5.3.3. Flat-Field Stability*

Long-term flat-field stability was investigated by obtaining between 5 and 10 dome flats in each of the WHIRC filters from April through 2008 July. Each flat was processed in the same manner, and the mean normalized to 1.0 over two regions away from the pupil ghost in the center of the field. The flats for each filter were then divided by a flat chosen as a reference, and the ratios were analyzed by obtaining statistics within seven $100 \times 100$ pixel subregions. The deviations from unity are typically less than 1% over the course of these 4 months (Fig. 14).

### 5.4. Ghosting

We required that secondary images must have peak fluxes that are at no more than $2 \times 10^{-4}$ of the primary images. Essentially, a star that is just under saturation should not have a detectable ghost, i.e., any ghost is less than the expected 3 $\sigma$ noise limit. We took images on 2008 July 15 of alpha Ser ($J = 0.83$, $H = 0.29$, and $K = 0.15$), a very bright star that saturates the field in the shortest integration. Several ghosts were found with peak fluxes $5 \times 10^{-7}$ to $2 \times 10^{-4}$ of the primary images. However, all met the relative faintness requirements with respect to the main star image (see Joyce 2008b).

FIG. 16.—Three color image ($J$, $H$, and $K_s$) of the edge-on galaxy, NGC 891, taken with WHIRC in 2008 September (*Image credit: D. Joyce/NOAO and M. Povich/University of Wisconsin*).

### 5.5. Photometric Quality

The photometric and flat-fielding performance of WHIRC was tested on the open cluster NGC 7790, which has six standard stars included in the listing of Hunt et al. (1998) under the name of AS 40 (Fig. 9). Their broadband magnitudes, as well as those from the 2MASS Point Source Catalog, are shown in Table 6. The published uncertainties for these standards are in the range 0.008–0.018 for the Hunt et al. catalog and 0.015–0.030 for the 2MASS catalog. This analysis will use the Hunt et al. numbers because of their lower uncertainty. Star 5 is problematic because it is sufficiently bright to push the WHIRC detector close to saturation, particularly in the broadband filters. It also has a companion approximately 3.2 mag fainter only 3.5″ away, which was almost certainly included in both the Hunt et al and 2MASS apertures, whereas it was easily isolated in the WHIRC images. In fact, the data show that the results for this star were typically 0.03–0.05 mag fainter than for the other stars, consistent with the published magnitudes being too bright. Thus for our photometric analysis, we exclude star 5.

On 2008 September 18 under photometric conditions, the NGC 7790 field was imaged through six filters ($J$, $H$, $K_s$, Pa$\beta$, Fe II, Br$\gamma$) to test the performance in both broad- and narrowband filters and as a function of wavelength. Nine images were taken in each filter, in a $3 \times 3$ grid pattern with a 30″ grid point separation. The integration times were 4 s and 40 s for the broad- and narrowband filters, respectively. The images, which had reference pixels removed, were corrected for nonlinearity and flat-field variations. We measured the photometry of the stars in both the unflattened (no flat column) and flat fielded (flat column) images. For each image, the standard deviation of the (WHIRC measurement, Table 6 value) magnitudes for stars 0–4 is calculated for each of the nine telescope pointings and reported in Table 7. The final row is the average of these standard deviations, with the flattened data representing the conclusions of this experiment. Because the five stars are in different positions on the detector, this is also a measure of the flat-fielding accuracy. Any error in the published magnitudes will contribute to the calculated uncertainty. Comparison of the five standard stars (stars 0–4) to each other demonstrates a

flat-fielding and photometric accuracy of better than 0.02 magnitudes in $J$, $H$, and $K_s$, as well as in the narrowband filters Pa$\beta$, Fe II, and Br$\gamma$.

### 5.6. WHIRC and WTTM Performance

WTTM is a tip-tilt optical system installed in the WIYN instrument rotator (Claver et al. 2003). Because WTTM was originally designed for use with an optical imager, it was modified from the design shown in Claver et al. for use with WHIRC. First, the ADC prisms were removed from the beam. Secondly, the beam splitter in front of the WHIRC mounting port, which was used to transmit a fraction of the science beam to the error sensing APD quad detector, has been replaced by a dichroic because the APD sensor and WHIRC wavelength ranges are exclusive. This increases the sensitivity of the APD sensor, which now receives almost all of the visible light.

Because WTTM is essentially a fast guider, sampling in the 50–200 Hz range, guide stars must be sufficiently bright ($R \sim 14.5$–$15.5$, depending on the seeing) to yield an acceptable signal at these fast sample rates. In addition, because the reference star signal must pass through the WTTM optics, the acquisition field is roughly the same as the WHIRC FOV, so not all science fields can take advantage of WTTM correction.

Performance tests to date suggest that WTTM correction can improve the image FWHM by 0.1–0.15″ under conditions of reasonable image quality (0.7–1.0″). Improvements under very good or very bad seeing conditions are mixed, although WTTM does appear to provide relatively uniform FWHM images under conditions of variable seeing. WTTM can also significantly reduce the effects of wind shake, which can be a problem with the very light weight WIYN telescope. Figure 15 illustrates the results of WTTM testing under light and strong wind conditions.

## 6. WHIRC: CONTEXT AND FUTURE PLANS

WHIRC has been delivered and integrated with the WIYN telescope. Observations taken almost monthly have resulted in a characterization of WHIRC's throughput, gain, readout noise, dark current, and image quality. These measured characteristics demonstrate that WHIRC has met its requirements. WHIRC was accepted by the WIYN observatory as a general use instrument in 2008 November. WHIRC is available for use by the general astronomical community through the NOAO application process.

In Table 8, WHIRC's capabilities are compared with some currently operating NIR cameras on 3–4 m class telescopes available to US astronomers. These performance values are collected from the observatory Web sites for the instruments as of 2009 November. Column (1) shows the telescopes and aperture size, instrument name and hemisphere. Column (2) is the year the instrument became available for community use. Column (3) lists the array format and wavelength coverage. Columns (4) and (5) are the pixel scale and FOV for the camera. Column (6) is $\Omega$ or the number of resolution elements in a single image FOV, calculated by dividing the FOV area by the area of the angular resolution element. Column (7) is the 10 $\sigma$ sensitivity limits in 1 minute (60 s) of integration time. Reported sensitivity limits for instruments are reported using different criteria at the different Web sites. In particular, the $\sigma$ level, integration time, and aperture size all vary. In an attempt to renormalize these for some common comparison, we adjusted the Web site reported numbers to 60 s of integration time and a 10 $\sigma$ level. These sensitivity limits should be treated as approximate. All sites apparently use aperture photometry, so we report the predicted WHIRC sensitivity limit with an aperture instead of PSF fitted photometry as well. The aperture sizes reported by the instruments are 3″ for NEWFIRM, 2.2″ for Flamingos, 1.6″ for WHIRC, 1.2″ for ISPI, may well cause some of the variation in the table. The SOAR/Spartan camera is undergoing commissioning and shakedown now, and it is too early for sensitivity measurements, so we leave these blank.

WHIRC's performance is well within the expected range of currently available NIR cameras. Of particular note, WHIRC has capabilities complementary to NEWFIRM and is suitable for high resolution imaging follow-up to NEWFIRM detections. In conclusion, WHIRC is well suited for studying the nearby universe, as demonstrated by the $J$, $H$, and $K_s$ image of the edge-on galaxy, NGC 891, taken by WHIRC in 2007 September (Fig. 16).[12]

The WHIRC project is grateful for the funding and in-kind contribution support from the Space Telescope Science Institute DDRF grants 82335, 92363, 90100, and 90101, the National Science Foundation grant 0504085, the WIYN Observatory, the University of Wisconsin, and the NOAO. M. Meixner and R. L. Doering were also supported by NASA NAG5-12595. Here we acknowledge the efforts of people not on the WHIRC team but who have assisted greatly with the commissioning and acceptance effort for WHIRC: Maureen Ellis (NOAO) for her excellent technical insights on the WHIRC detector and MONSOON issues on pickup noise and for leading the solving of the noise problems; Bob Marshall (NOAO) for his guidance of the software design; Mark Hunten, Peter Moore, and Ron George for their support of the MONSOON detector head electronics and power supply; Bill Ditsler (NOAO) and Ken Don (NOAO) for support on the thermal vacuum and mechanical aspects of the WHIRC cryostat. We appreciate the technical feedback of our design review board members and of colleagues Richard Green, Mike Merrill, and Nick Buchholz of NOAO and John MacKenty of STScI. We are grateful to WHIRC science team members who provided science use cases for the proposals and filter definitions: Mike Regan, Andrew

[12] A Web page on WHIRC status can be referenced for future use: http://www.noao.edu/kpno/WHIRC_instrument.htm.

Fruchter, and Massimo Stiavelli of STScI; Jay Gallagher and Linda Sparke of the University of Wisconsin who helped define the redshifted narrowband set; James Rhoads and Sangheeta Malhotra of Arizona State University, who defined the low airglow filter; Catherine Pilachowski of Indiana University; Remy Indebetouw of University of Virginia; and Peter van Dokkum of Yale. Commissioning observations have been collected and analyzed by several individuals not on the WHIRC team. Matt Povich (University of Wisconsin; now Penn State) estimated the plate scale and produced the GLIMPSE GC-1 press release images. Heidi Schweiker Christopher provided guidance on completing the WHIRC commissioning and leading the integration of WTTM and WHIRC. Lynn Carlson (Johns Hopkins University) assisted with the 2008 September observations.

## REFERENCES

Anderson, D., Burge, J., Ketelson, D., Martin, B., West, S., Poczulp, G., Richardson, J., & Wong, W. 1994, Proc. SPIE, 2199, 193

Barkhouser, R., Smee, S. A., & Meixner, M. 2004, Proc. SPIE, 5492, 921

Benjamin, R. A., et al. 2003, PASP, 115, 953

Buchholz, N. C., & Daly, P. N. 2004, Proc. SPIE, 5496, 364

Carney, B. W., Lee, J.-W., & Dodson, B. 2005, AJ, 129, 656

Churchwell, E., et al. 2009, PASP, 121, 213

Claver, C. F., Corson, C., Gomez, R., Daly, P., Dryden, D., & Abareshi, B. 2003, Proc. SPIE, 4837, 438

Doering, R. L., & Meixner, M. 2009, AJ, 138, 780

Fowler, A., & Gatley, I. 1990, ApJ, 353, L 33

Harbeck, D., Gallagher, J. S.III, & Grebel, E. K. 2004, AJ, 127, 2711

Hartmann, L., Hinkle, K., & Calvet, N. 2004, ApJ, 609, 906

Hunt, L. K., Mannucci, F., Testi, L., Migliorini, S., Stanga, R. M., Baffa, C., Lisi, F., & Vanzi, L. 1998, AJ, 115, 2594

Hunten, M., Garcia, J., Moore, P., Rahmer, G., & Schmidt, R. 2004, Proc. SPIE, 5499, 481

Indebetouw, R., Watson, C., Johnson, K. E., Whitney, B., & Churchwell, E. 2003, ApJ, 596, L 83

Johns, M., & Blanco, D. 1994, Proc. SPIE, 2199, 2

Joyce, R. 2008a, WHIRC Report II: Signal, Mean-Variance (Tucson, AZ: National Optical Astronomical Observatory), http://www.noao.edu/kpno/manuals/whirc/reports.html

———. 2008b, WHIRC Report IV: Ghost Images (Tucson, AZ: National Optical Astronomical Observatory), http://www.noao.edu/kpno/manuals/whirc/reports.html

Joyce, R., Meixner, M., Miller, T., & Churchwell, E. 2009, WIYN High Resolution Infrared Camera (WHIRC) User's Guide (Tucson, AZ: National Optical Astronomical Observatory), http://www.noao.edu/kpno/manuals/whirc/manuals.html

McPherson, A. M., et al. 2006, Proc. SPIE, 6267, 7

Meixner, M., Young Owl, R., & Leach, R. W. 1999, PASP, 111, 997

Meixner, M., et al. 2004, Proc. SPIE, 5492, 1440

Meixner, M., et al. 2008, Proc. SPIE, 7014, 101

Raytheon Vision Systems 2004, User's Guide and Operating Manual for the VIRGO-2K 2048x2048 SWIR, HgCdTe IRFPA, Readout Model #: SB-301, by Astronomy Team, 02-0374MAN

Roddier, F., Northcott, M., & Graves, J. E. 1991, PASP, 103, 131

Roddier, N., Blanco, D., Goble, L., & Roddier, C. 1995, Proc. SPIE, 2479, 364

Speck, A. K., Meixner, M., Jacoby, G. H., & Knezek, P. M. 2003, PASP, 115, 170

Tokunaga, A. T., Simmons, D. A., & Vacca, W. D. 2002, PASP, 114, 180